Analytical Model of Modular Spoke-Type Permanent Magnet Machines for In-Wheel Traction Applications

Hengliang Zhang, Wei Hua, David Gerada, Zeyuan Xu, Chris Gerada

***Abstract*—This paper proposes an analytical model of modular spoke-type permanent magnet (MSTPM) machines based on air-gap field modulation (AFM) theory. Firstly, a fundamental AFM model of open-circuit MSTPM machines is introduced. The open-circuit air-gap field of MSTPM machines is determined by three fundamental elements including the primitive magnetizing magnetomotive force (MMF) produced by permanent magnet (PM), and two modulators which consist of stator and rotor permeance. The analytical MMF excited by PM (PM-MMF) can be calculated by using magnetic circuit method, while the stator and rotor permeance models are developed based on relative permeance (RP) method. Thereafter, a general model is proposed to calculate the open-circuit back electromotive force (EMF) of MSTPM machines. Further, the winding inductance model is established on the basis of equivalent magnetic circuit method and RP model. Finally, the machine performance is predicted by the analytical model, and verified by both finite element analysis (FEA) and experimental results.**

***Index Terms*—Air-gap field modulation, AC machines, spoke-type PM machines, in-wheel traction.**

NOMENCLATURE

θ	Air-gap position
μ_0	Permeability of vacuum
ω	Rotor mechanical speed (rad/s)
$\Lambda_r(\theta, t)$	Relative rotor permeance at (position θ, moment t)
Λ_{r0}	Average relative rotor permeance
Λ_{s0}	Average relative stator permeance
Λ_{r1}	Amplitude of fundamental relative rotor permeance
$\Lambda_s(\theta, t)$	Relative stator permeance at (position θ, moment t)
$B_r(\theta, t)$	Radial air-gap flux density at (position θ, moment t)
B_{ho}	The h_o^{th} harmonic of air-gap flux density
$e_c(t)$	Back-EMF of a single coil at moment t
e_k	The k^{th} phase back-EMF
$e_{k\text{-}ho}$	The harmonic of the k^{th} phase back-EMF induced by the ho^{th} harmonic of flux density
$F(\theta, t)$	Magnetic potential at (position θ, moment t)
F_{PM}	Amplitude of PM-MMF
g	Length of air-gap
h_l	The spatial order of fundamental position-varying inductance
k_d	Winding distribution factor
k_p	Winding pitch factor
k_w	Winding factor
l	Effective stack length
l_{sp}	Length of stator pitch
l_{rp}	Length of rotor pitch
$L_{s\text{-}air\text{-}av}$	Average air-gap self-inductance per phase
$L_{s\text{-}av}$	Average self-inductance per phase
L_m	Phase-to-phase mutual-inductance
$L_{m\text{-}air}$	Air-gap mutual-inductance per phase
$L_{m\text{-}slot}$	Slot leakage mutual-inductance per phase
$L_{s\text{-}slot}$	Slot leakage self-inductance per phase
L_s	Self-inductance per phase
N_c	Number of turns per coil
N_p	Number of turns per phase
N_{pm}	Magnet number
N_{rt}	Rotor tooth number
N_{st}	Stator tooth number
p	Rotor pole number
p_e	Pole-pair number of excitation source
Q	Stator slot number
r	Radius of the center circle of air-gap
w_r	Width of rotor slot
w_s	Width of stator slot

This work was supported in part by the National Science Foundation of China under Grant 51777032, in part by the Key R&D Program of Jiangsu Province under Grant BE2019073, and in part by the Scientific Research Foundation of Graduate School of Southeast University under Grant YBJJ1834.

Hengliang Zhang, and Wei Hua are with the School of Electrical Engineering, Southeast University, Nanjing, China (email: zhanghl2019@163.com, huawei1978@seu.edu.cn).

David Gerada, Zeyuan Xu, and Chris Gerada are with University of Nottingham, NG7 2RD, UK (email: David.Gerada@nottingham.ac.uk, Zeyuan.Xu@nottingham.ac.uk, Chris.Gerada@nottingham.ac.uk).

I. INTRODUCTION

In recent years, in-wheel traction (IWT) machines have been increasingly hot research topics due to the high torque density, and excellent system efficiency [1]-[3]. It is believed that the electric vehicles (EVs) driven by IWT machines are ideal candidates of future transportation. According to the available literature, a variety of machine topologies have been designed for the IWT applications, including the switched reluctance (SR) machines [4], the surface permanent magnet (SPM) machines [5], the V-shaped interior permanent magnet (IPM) machines [2], the flux-switching permanent magnet (FSPM) machines [1], the magnetic gear (MG) machines [6], etc.

In [7], [8], the MSTPM machines are found to feature a higher machine efficiency, a better flux-weakening performance, and a stronger over-load capability than conventional flux-switching permanent magnet (FSPM)

machines, and surface-mounted permanent magnet (SPM) machines used in IWT applications. It is certain that the MSTPM machines deserve more research attentions, especially in the field of IWT applications.

By now, an analytical prediction of air-gap field in MSTPM machines has been derived based on conformal mapping method [7]. The design considerations of the MSTPM machines were discussed in [8], where the elimination of even-order harmonics and unbalanced magnetic force, and the optimization of rotor tooth width were involved. Further, the back-EMF waveform, and possible stator-slot/rotor-pole combinations of MSTPM machines were analyzed in [9]. The influence of magnetization mode on machine performance was investigated in [10], [11]. However, a general analytical model of MSTPM machines has not been built in existing literature, with magnetic field, back-EMF, and winding inductance included.

On the other hand, the AFM theory has been used in the analysis of a variety of kinds of electrical machines [12], [13], including FSPM machines [14], [15], flux-reversal permanent magnet (FRPM) machines [16], [17], SPM machines [18], fractional-slot concentrated-winding (FSCW) vernier permanent magnet (VPM) machines [19], partitioned-stator FSPM machines [20], etc. A general AFM theory has been built in [12], where a basic unit motor is normalized into a cascade of three key elements, namely the excitation source (primitive magneto-motive force), the modulator (salient pole/short circuit coil/flux guide) and the filter (armature winding). It has been proved that, the general AFM theory is valid for all electromagnetic machines, irrespective of DC or AC machines, salient or non-salient machines, sinusoidal or rectangular current driven machines, etc., with respect to both the qualitative and quantitative analyses associated with clear physical meanings. Further, the AFM theory has also been successfully used in the topology exploration of novel electrical machines [20], [21]. Hence, it is certain that an analytical model of the MSTPM machines can be built based on the general AFM theory.

Since the MSTPM machines have different structures from traditional electrical machines, and different magnetization modes of MSTPM machines lead to different stator/rotor structures, resulting in different winding inductance formulae [23], [24], it is necessary to build the winding inductance model to guide the future design of MSTPM machines. Besides, the MSTPM machine is one type of FSCW machines, of which the main winding inductance is the slot leakage component and air-gap component [25], [26]. Hence, special attention should be focused on the slot leakage and air-gap inductances of MSTPM machines.

This paper is arranged as follows. A mathematical model of air-gap open-circuit field in MSTPM machines with different magnetization modes is set up on the basis of AFM theory and RP method in Section II. Then, an analytical model of phase back-EMF is developed in Section III, where the relationships between spatial field harmonics and temporal back-EMF harmonics are investigated. Thereafter, the winding inductance of the proposed machines is analyzed in Section III. Further, the machine performance is analytically predicted according to the foregoing models. Finally, two-dimensional (2D) finite element analysis (FEA) projects are built, and corresponding prototyped machines are assembled and tested to verify the analytical results.

II. AFM IN MSTPM MACHINES

In this section, the AFM model of MSTPM machines is built. Some assumptions should be obeyed: 1) no 3D end-effect; 2) the infinite permeability of silicon steel sheets; 3) the same permeability of both magnets and nonmagnetic support cells as vacuum; 4) ignoring tangential air-gap field component.

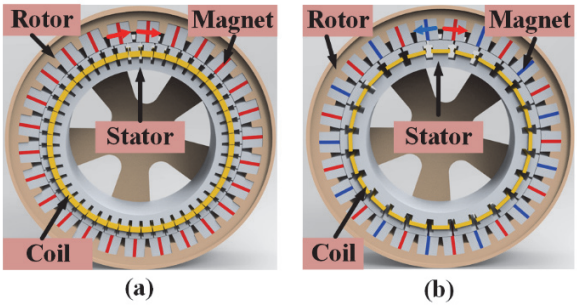

Fig. 1. Magnetization modes of MSTPM machines. (a) M-I. (b) M-II.

A. Machine Topology

As shown in Fig. 1, there are two different magnetization modes for MSTPM machines, which in this paper are referred to as M-I and M-II modes. The only difference is that the magnetization directions of two adjacent magnets are same in M-I machines, and reversal in M-II machines. Correspondingly, Figs. 2(a) and 2(b) show the PM flux paths of these two magnetization modes.

It can be found that under M-I mode, the magnetic polarity reverses in every rotor tooth, namely N-S-N-S…, whereas under M-II mode, the magnetic polarity reverses in every two rotor teeth namely S-N-N-S…, which results in distinct models as follows. Hence, the M-I MSTPM machines are equivalent to the topology shown in Fig. 2(c), while the M-II MSTPM machines are equivalent to the topology of Fig. 2(d).

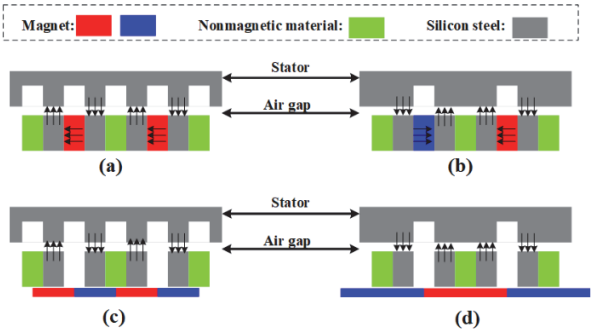

Fig. 2. PM flux paths in MSTPM machines. (a) M-I. (b) M-II. (c) Equivalent M-I. (d) Equivalent M-II.

B. General AFM Model

From Figs. 2(c) and 2(d), it can be observed that the open-circuit air-gap field of MSTPM machines is due to the modulation of the primitive PM-MMF by both rotor and stator. Hence, the PM-MMF, the stator permeance, and the rotor permeance are investigated in this paper, respectively.

The MSTPM machines is one kind of rotor-magnet (RM) FSCW machine where magnets are housed on the rotor, which means the PM-MMF is rotary. Based on Fourier series, the PM-MMF is expressed by

$$F(\theta,t)=\sum_{i=1}^{\infty}F_i\cos[ip_e(\theta+\omega t)] \tag{1}$$

where p_e is pole-pair number of PM-MMF, ω is mechanical rotational speed, θ is air-gap position, and t is time.

For M-I machines, the pole-pair number p_e is

$$p_e=N_{pm} \tag{2}$$

For M-II machines, p_e yields

$$p_e=\frac{N_{pm}}{2} \tag{3}$$

Further, the relative stator permeance of the MSTPM machines can be expressed as

$$\Lambda_s(\theta,t)=\sum_{j=0}^{\infty}\Lambda_{sj}\cos(jN_{st}\theta) \tag{4}$$

where N_{st} is the number of stator slots.

In [9], it is found that the pole-pair number p_e and the rotor tooth number N_{rt} of M-I MSTPM machines should be constrained by (5) in order to achieve maximum torque.

$$N_{rt}=2p_e \tag{5}$$

As for M-II MSTPM machines, according to [11], it is found that the non-magnetic parts, which are sandwiched by rotor teeth, should be removed to achieve the maximum torque. Hence, in this paper, the analysis of the M-II MSTPM machines is based on the optimal structure shown in Fig. 3. Therefore, the pole-pair number p_e and the rotor tooth number N_{rt} of the M-II MSTPM machines is constrained by (5) as well.

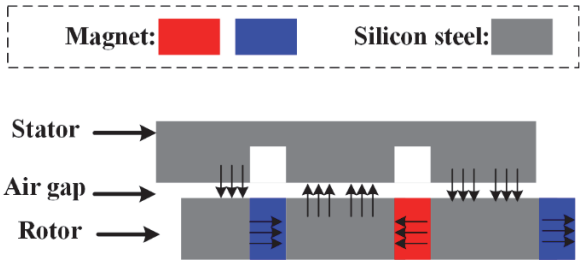

Fig. 3. The optimal structure of the M-II MSTPM machines.

Then, the relative rotor permeance can be expressed by

$$\Lambda_r(\theta,t)=\sum_{k=0}^{\infty}\Lambda_{rk}\cos[2kp_e(\theta+\omega t)] \tag{6}$$

Hence, the open-circuit air-gap flux density yield

$$B_r(\theta,t)=\frac{\mu_0}{g}F(\theta,t)\Lambda_s(\theta,t)\Lambda_r(\theta,t)=$$
$$\frac{\mu_0}{g}\sum_{i=1}^{\infty}\sum_{j=0}^{\infty}\sum_{k=0}^{\infty}\frac{F_i\Lambda_{sj}\Lambda_{rk}}{4}\{$$
$$\cos[(ip_e\pm jN_{st}+2kp_e)\theta+(i+2k)p_e\omega t]+$$
$$\cos[(ip_e\pm jN_{st}-2kp_e)\theta+(i-2k)p_e\omega t]\} \tag{7}$$

C. PM-MMF

In the AFM model of MSTPM machines, the PM-MMF is the square wave shown in Fig. 4, which is different from the conventional MMF-permeance method [8], [11]. In the conventional MMF-permeance method, the PM-MMF waveform always carries the harmonic information of rotor structure by assigning the width of wave crest of PM-MMF. However, in the AFM model, the harmonic information of rotor structure is carried by the relative rotor permeance. The PM-MMF waveform only carries the information on amplitude and pole-pair of the MSTPM machines. The amplitude of the PM-MMF F_{PM} can be calculated by using equivalent magnetic circuit model of two types of MSTPM machines in [11].

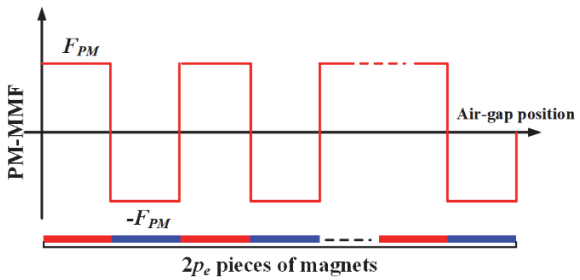

Fig. 4. The PM-MMF of MSTPM machines.

Compared to the conventional MMF-permeance method, the proposed model provides more accurate information on field harmonics because of the more accurate rotor information. In Fig. 5, the air-gap field harmonic spectra of an M-I MSTPM machine are calculated by the FEA model, the MMF-permeance method, and the proposed model, respectively, while the corresponding calculation errors of the MMF-permeance method and the proposed model are shown in Fig. 6. It is found that the results calculated by the MMF-permeance method feature a bigger error.

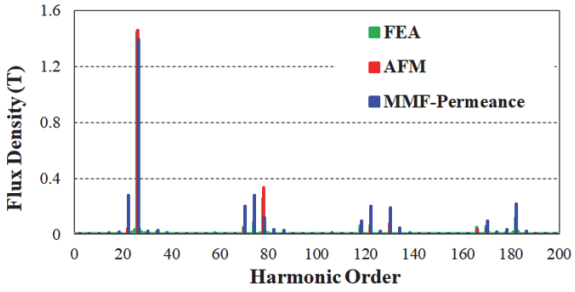

Fig. 5. The air-gap field harmonic spectra of an M-I MSTPM machine calculated by FEA model, MMF-permeance method, and the proposed model.

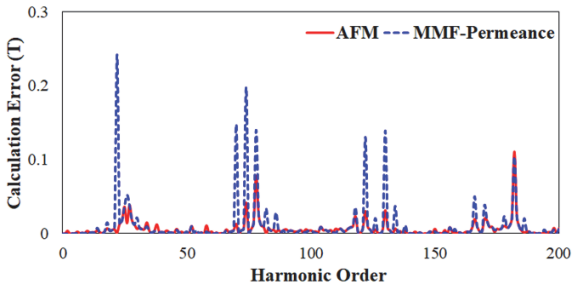

Fig. 6. The calculation errors of the MMF-permeance method, and the proposed model.

D.Relative Stator Permeance

Since only the radial flux-density component is considered in the AFM model, a RP model rather than a complex RP model is built, decreasing the complexity of stator permeance model [27]-[31].

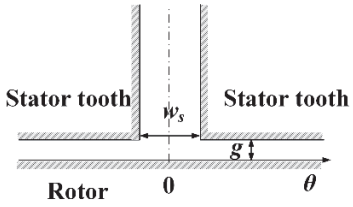

Fig. 7. Assumed infinite deep stator slot.

As shown in Fig. 7, the stator slot is assumed as an infinite deep rectilinear slot. According to [32], at the center circle of air-gap, the RP of the infinite deep stator slot is

$$\Lambda_s(\theta,t)=\begin{cases}1-\beta_1-\beta_1\cos\left(\dfrac{\pi\theta}{0.8\theta_{so}}\right) & 0\le\theta\le 0.8\theta_{so}\\ 1 & 0.8\theta_{so}\le\theta\le\dfrac{\theta_{sp}}{2}\end{cases} \tag{8}$$

$$\beta_1=\frac{1}{2}-\frac{1}{2\sqrt{1+\left(\dfrac{w_s}{2g}\right)^2(1+v^2)}} \tag{9}$$

$$\theta_{so}=\frac{w_s}{r} \tag{10}$$

$$\theta_{sp}=\frac{l_{sp}}{r} \tag{11}$$

where, v can be obtained from

$$\frac{g\pi}{2w_s}=\frac{1}{2}\ln\left(\frac{\sqrt{a^2+v^2}+v}{\sqrt{a^2+v^2}-v}\right)+\frac{2g}{w_s}\arctan\left(\frac{2gv}{w_s\sqrt{a^2+v^2}}\right) \tag{12}$$

$$a^2=1+\left(\frac{2g}{w_s}\right)^2 \tag{13}$$

Based on equations (8)-(13), the relative stator permeance in the half stator pitch can be calculated. Then the whole stator permeance can be extended based on the symmetric condition.

The single stator pitch of the MSTPM machines with Q stator-slot is

$$l_{sp}=\frac{2\pi r}{Q} \tag{14}$$

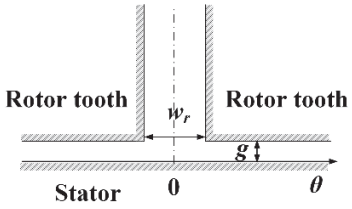

Fig. 8. Assumed infinite deep rotor slot.

E. Rotor Permeance

Similarly, the rotor slot is also assumed as an infinite deep rectilinear slot as shown in Fig. 8. At the center circle of air-gap, the RP of the infinite deep rotor slot is

$$\Lambda_r(\theta,t)=\begin{cases}1-\beta_2-\beta_2\cos\left(\dfrac{\pi\theta}{0.8\theta_{ro}}\right) & 0+\omega t\le\theta\le 0.8\theta_{ro}+\omega t\\ 1 & 0.8\theta_{ro}+\omega t\le\theta\le\dfrac{\theta_{rp}}{2}+\omega t\end{cases} \tag{15}$$

$$\beta_2=\frac{1}{2}-\frac{1}{2\sqrt{1+\left(\dfrac{w_r}{2g}\right)^2(1+v^2)}} \tag{16}$$

$$\theta_{ro}=\frac{w_r}{r} \tag{17}$$

$$\theta_{rp}=\frac{l_{rp}}{r} \tag{18}$$

where, v can be calculated by

$$\frac{g\pi}{2w_r}=\frac{1}{2}\ln\left(\frac{\sqrt{a^2+v^2}+v}{\sqrt{a^2+v^2}-v}\right)+\frac{2g}{w_r}\arctan\left(\frac{2gv}{w_r\sqrt{a^2+v^2}}\right) \tag{19}$$

$$a^2=1+\left(\frac{2g}{w_r}\right)^2 \tag{20}$$

Based on equations (15)-(20), the relative rotor permeance in the half rotor pitch can be calculated, and the whole rotor permeance is extended according to the geometric symmetry.

For the MSTPM machines with p_e pole-pair PM-MMF, the single rotor pitch is

$$l_{rp}=\frac{\pi r}{p_e} \tag{21}$$

III. Phase Back-EMF Model

In MSTPM machines, the PM flux penetrating a coil is

$$\varphi_c(t)=N_c\int_{-\frac{\theta_{sp}}{2}}^{\frac{\theta_{sp}}{2}}B_r(\theta,t)rld\theta \tag{22}$$

where N_c is the number of turns per coil, r is the radius of the center circle of air-gap, and l is the effective stack length.

Based on (7), the coil back-EMF of MSTPM machines is

$$e_c(t)=-\frac{d\varphi_c(t)}{dt}=N_c\omega rl\frac{\mu_0}{g}\sum_{i=1}^{\infty}\sum_{j=0}^{\infty}\sum_{k=0}^{\infty}\int_{-\frac{\theta_{sp}}{2}}^{\frac{\theta_{sp}}{2}}\frac{F_i\Lambda_{sj}\Lambda_{rk}}{4}\{$$
$$(i+2k)p_e\sin[(ip_e\pm jN_{st}+2kp_e)\theta+(i+2k)p_e\omega t]+$$
$$(i-2k)p_e\sin[(ip_e\pm jN_{st}-2kp_e)\theta$$
$$+(i-2k)p_e\omega t]\}d\theta \tag{23}$$

From (23), it is found that the back-EMF frequency in MSTPM machines is determined by the pole-pair number p_e, and the rotor mechanical speed ω. Further, each harmonic of coil back-EMF is induced by different spatial field harmonics, which means the back-EMF in MSTPM machines is caused by AFM phenomenon. The relationship between the spatial field and temporal back-EMF harmonics in MSTPM machines is determined by the pole-pair number p_e, stator tooth number N_{st}, and rotor tooth number N_{rt}.

Consequently, the electrical speed ω_e of coil back-EMF is

$$\omega_e = (i \pm 2k)p_e\omega \tag{24}$$

Hence, even-order harmonics will not appear in the back-EMF of ideal MSTPM machines whose PM-MMF waveforms are square waves. However, some even-order harmonics still exist in MSTPM machines caused by the permeability difference between magnets and nonmagnetic support cells, as reported in [8]. Since the magnets and nonmagnetic support cells have been assumed with the same permeability as vacuum, the even-order harmonics are ignored in this paper.

The relationship between spatial and temporal harmonics is concluded in Table I. The rotation direction of back-EMF harmonic is determined by multiplying electrical speed and field harmonic order.

TABLE I
RELATIONSHIP BETWEEN SPATIAL AND TEMPORAL HARMONICS IN MSTPM MACHINES

Back-EMF harmonic order	Electrical speed	Field harmonic order
1	$p_e\omega$	$p_e \pm jN_{st}$
	$-p_e\omega$	$-p_e \pm jN_{st}$
3	$3p_e\omega$	$3p_e \pm jN_{st}$
	$-3p_e\omega$	$-3p_e \pm jN_{st}$
	…	
k	$kp_e\omega$	$kp_e \pm jN_{st}$
	$-kp_e\omega$	$-kp_e \pm jN_{st}$

Hence, the temporal k^{th} back-EMF harmonic induced by the ho^{th} flux density harmonic can be obtained by

$$e_{k-ho} = p_e \frac{2k\omega N_p r l k_p k_d B_{ho}}{h_o} \tag{25}$$

where k_p is the winding pitch factor, k_d is the winding distribution factor, B_{ho} is the amplitude of the ho^{th} flux density harmonic.

The total k^{th} back-EMF harmonic e_k is

$$e_k = \sum_{h_o} e_{k-ho} \tag{26}$$

IV. WINDING INDUCTANCE IN MSTPM MACHINES

Since the MSTPM machines belongs to the FSCW-PM machines, the winding inductance can be divided into two parts: 1) slot leakage component; 2) air-gap component.

F. Slot Leakage Component

As the MSTPM machines for IWT applications are equipped with external rotor, the stator slot is normalized as the tapered slot shown in Fig. 9. In FSCW machines with double-layer windings, each winding slot is made up of two conductors shown in Fig. 9(a), namely as conductor 1 and conductor 2. In FSCW machines with single-layer windings, each winding slot is made up of one conductor shown in Fig. 9(b), namely as conductor 3. For both double- and single-layer FSCW machines, calculating the leakage permeance of single slot is the key step in the prediction of slot leakage inductance.

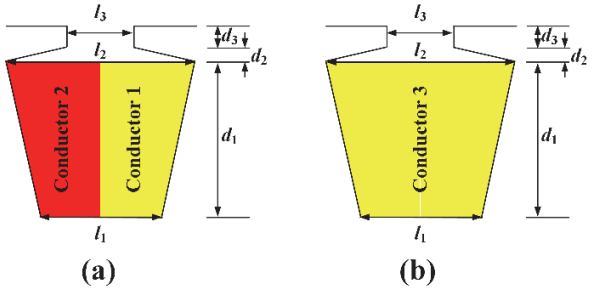

Fig. 9. Tapered slot of MSTPM machines for in-wheel tractions.

Each armature slot can be divided into three regions, i.e., the conductor region, the trapezoid region, and the rectangular region, whose height is d_1, d_2, and d_3, respectively.

For the conductor region whose height is d_1, the leakage permeance is [33]

$$p_c = \mu_0 \frac{d_1}{l_2} \left[\frac{\left(\frac{l_2}{l_1}\right)^2 - \frac{1}{4}\left(\frac{l_2}{l_1}\right)^4 - \ln\left(\frac{l_2}{l_1}\right) - \frac{3}{4}}{\left(1 - \frac{l_2}{l_1}\right)\left(1 - \left(\frac{l_2}{l_1}\right)^2\right)^2} \right] \tag{27}$$

For the trapezoid region whose height is d_2, the leakage permeance is

$$p_t = \mu_0 \frac{d_2}{l_2 - l_3} \ln\left(\frac{l_2}{l_3}\right) \tag{28}$$

For the rectangular region whose height is d_3, the leakage permeance is

$$p_r = \mu_0 \frac{d_3}{l_3} \tag{29}$$

For single-layer machines, the slot leakage self-inductance per phase is

$$L_{s-slot} = \frac{2Q}{m} N_c^2 l (p_c + p_t + p_r) \tag{30}$$

The slot leakage mutual-inductance per phase is

$$L_{m-slot} = 0 \tag{31}$$

For double-layer machines with odd phase number m, the slot leakage self-inductance per phase is

$$L_{s-slot} = N_c^2 l(p_c + p_t + p_r)(\frac{4Q}{m} - 4N_{sub}) \quad (32)$$

The slot leakage mutual-inductance per phase is

$$L_{m-slot} = -2N_{sub}N_c^2 l(p_c + p_t + p_r) \quad (33)$$

For double-layer machines with even phase number m, the slot leakage self-inductance per phase is

$$L_{s-slot} = N_c^2 l(p_c + p_t + p_r)(\frac{4Q}{m} - 2N_{sub}) \quad (34)$$

The slot leakage mutual-inductance per phase is

$$L_{m-slot} = -N_{sub}N_c^2 l(p_c + p_t + p_r) \quad (35)$$

where N_{sub} is the number of the sub-machine that a machine can be divided into, being the greatest common divisor (GCD) of Q and p_e, as expressed by

$$N_{sub} = GCD(Q, p_e) \quad (36)$$

G.Air-gap Component

The air-gap component consists of two parts which are average inductance and position-varying inductance. The average component can be obtained on the basis of the average relative rotor and stator permeance.

The average component of air-gap self-inductance is

$$L_{s-air-av} = N_c^2 \frac{\pi r l \mu_0}{mg} \Lambda_{r0}\Lambda_{s0} \quad (37)$$

Based on equations (30), (32), (34), (37) the average self-inductance of phase winding can be obtained by

$$L_{s-av} = L_{s-slot} + L_{s-air-av} \quad (38)$$

For the position-varying component of self-inductance, only the fundamental position-varying inductance is considered, whose spatial order is

$$h_l = N_{rt} \quad (39)$$

Then, the amplitude of position-varying component can be calculated by

$$L_{s-air-va} = N_c^2 \frac{\pi r l \mu_0}{mg} k_w \Lambda_{r1}\Lambda_{s0} \quad (40)$$

where Λ_{r1} is the fundamental amplitude of the relative rotor permeance.

Hence, the self-inductance per phase is

$$L_s = L_{s-av} + L_{s-air-va}\sin(N_{rt}\theta) \quad (41)$$

Since the mutual-inductance is much less than the self-inductance, only the average mutual-inductance is considered in this paper. In FSCW machines with single-layer windings, the air-gap mutual-inductance is

$$L_{m-air} = 0 \quad (42)$$

In FSCW machines with double-layer windings, the average air-gap mutual-inductance is

$$L_{m-air} = \begin{cases} -\frac{N_{sub}}{2} N_c^2 \frac{\pi r l \mu_0}{Qg} \Lambda_{r0}\Lambda_{s0} & m\ is\ odd \\ -\frac{N_{sub}}{4} N_c^2 \frac{\pi r l \mu_0}{Qg} \Lambda_{r0}\Lambda_{s0} & m\ is\ even \end{cases} \quad (43)$$

Finally, the phase-to-phase mutual inductance is

$$L_m = L_{m-slot} + L_{m-air} \quad (44)$$

V. VERIFICATION

In this section, the electromagnetic performance of two M-I and M-II MSTPM machines for IWT applications are predicted by the proposed analytical model. Since the saturation phenomenon is ignored, the on-load performance is predicted according to the analytical open-circuit results. Then, the analysis is verified by both the FEA-predicted and experimental results. The key parameters are listed in Table II.

TABLE II
KEY PARAMETERS OF MSTPM MACHINES

Parameter	M-I MSTPM	M-II MSTPM
Magnet type	N35SH	
Magnet length	23mm	14.7mm
Magnet thickness	3.4mm	7.4mm
Silicon steel sheet	50WW600	
Q	48	24
Phase number	3	
Winding layer	Double-layer	
N_c	3	6
N_{pm}	26	
Outer radius	138mm	
g	0.5mm	
l	45mm	
l_1	3.4 mm	6.6 mm
l_2	6 mm	13.2 mm
l_3	1 mm	5 mm
d_1	21 mm	25 mm
d_2	0 mm	0 mm
d_3	2.5 mm	2.5 mm
r	114.8 mm	122.8 mm
w_r	3.4 mm	8.2 mm
w_s	1 mm	5 mm
DC-voltage	72V	
Rated current (RMS)	30A	
Rated speed	480r/min	

A. Experimental Platform

In Figs. 10 and 11, the 48s/52p M-I and 24s/26p M-II MSTPM machines are illustrated. In both machines, rotor modules are inserted into wheel rims using dovetail slot structure, which results in a high integrity. The interstices between the modular rotors and the rim are filled by anaerobic adhesive to improve structural stability.

As shown in Fig. 12, the experimental platform is made up of the prototype machine, the load (a magnetic powder brake), the

digital oscilloscope (Agilent MSO-X 3024A), the three-phase permanent-magnet synchronous machine (PMSM) controller, and the DC power supply (KIKUSUI PAT250-32T).

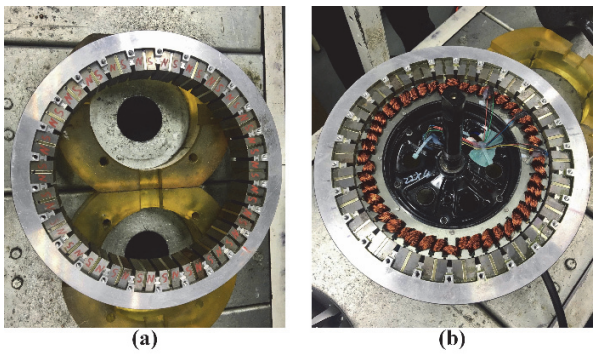

Fig. 10. The 48s/52p M-I MSTPM prototype machine. (a) Rotor (b) Stator and rotor.

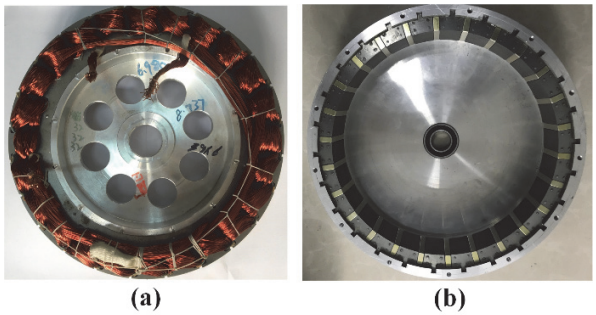

Fig. 11. The 24s/26p M-II MSTPM prototype machine. (a) Stator. (b) Rotor.

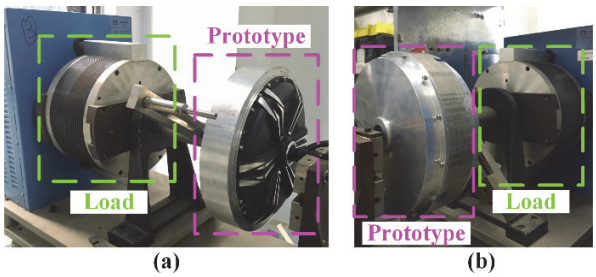

Fig. 12. Experimental platforms. (a) 48s/52p M-I MSTPM machine. (b) 24s/26p M-II MSTPM machine.

B. Open-Circuit Air-gap Flux Density

As described in the aforementioned analytical model, the 48-slot/52-pole (48s/52p) M-I MSTPM machine is normalized as the modulation of the PM-MMF, the rotor permeance, and the stator permeance shown in Figs. 13-15. The amplitude of the PM-MMF is derived based on the equivalent magnetic path model, which is 490.6 A. The air-gap flux density is further calculated by (7), as shown in Fig. 16. The analytical results are compared with the 2D-FEA-predicted results in Fig. 17 and Table III. According to Table I, the 26-th and 74-th spatial harmonics are the dominant harmonics inducing the fundamental back-EMF in 48s/52p MSTPM machines. It is found that the analytical 26-th harmonic amplitude is very close to the 2D-FEA results, where the error is less than 1%. Although analytical and FEA-predicted 74-th harmonics are different, this difference is acceptable since they only produce little amount of fundamental back-EMF.

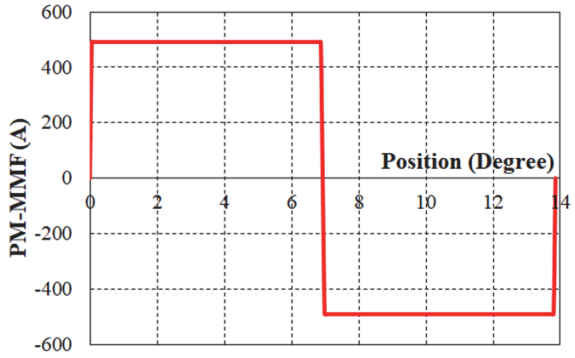

Fig. 13. The PM-MMF waveform in the 48s/52p M-I MSTPM machine.

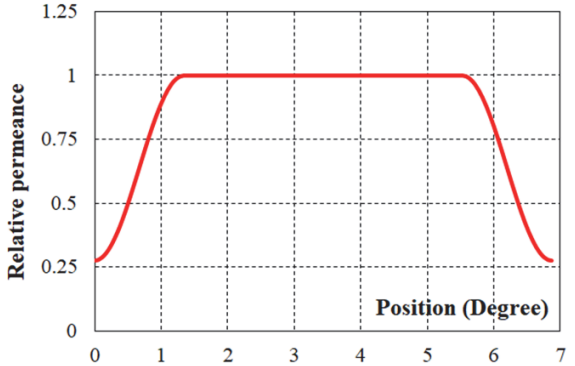

Fig. 14. The relative rotor permeance in the 48s/52p M-I MSTPM machine (one rotor pitch).

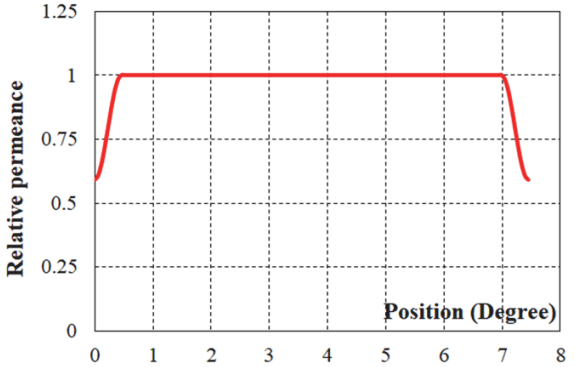

Fig. 15. The relative stator permeance in the 48s/52p M-I MSTPM machine (one stator pitch).

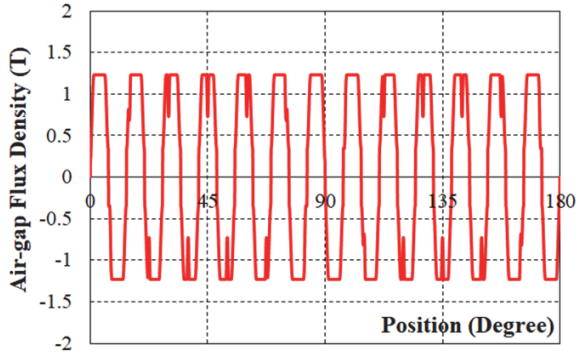

Fig. 16. The air-gap flux density in the 48s/52p M-I MSTPM machine.

TABLE III
SPATIAL HARMONICS IN 48S/52P M-I MSTPM MACHINE

Harmonic order	Analytical	2D-FEA
26	1.46 T	1.45 T
74	0.04 T	0.08 T

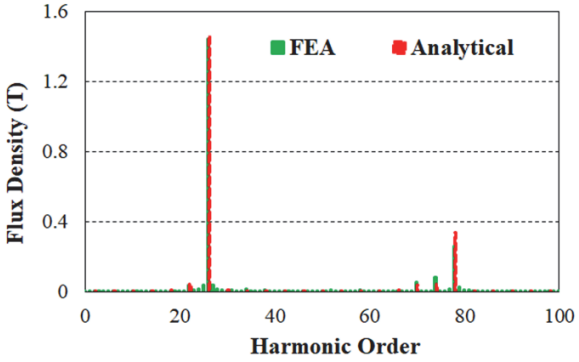

Fig. 17. The air-gap spatial harmonic spectra of the 48s/52p M-I MSTPM machine.

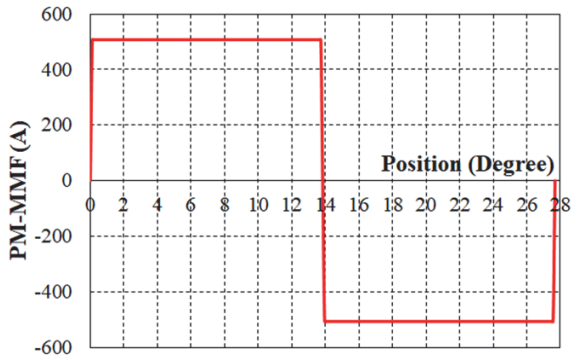

Fig. 18. The PM-MMF waveform in the 24s/26p M-II MSTPM machine.

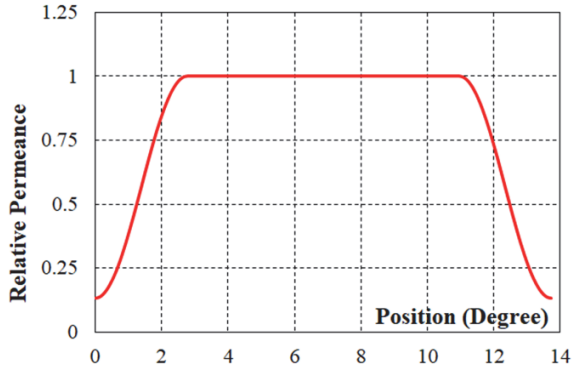

Fig. 19. The relative rotor permeance in the 24s/26p M-II MSTPM machine (one rotor pitch).

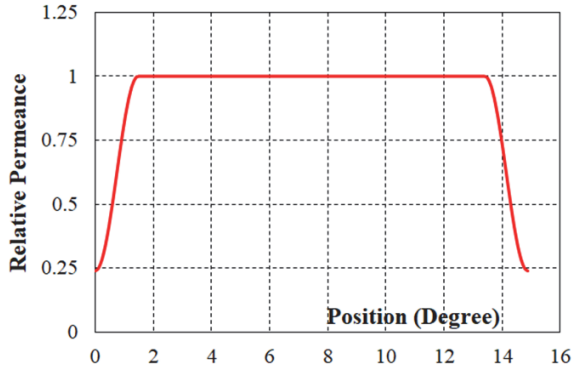

Fig. 20. The relative stator permeance in the 24s/26p M-II MSTPM machine (one stator pitch).

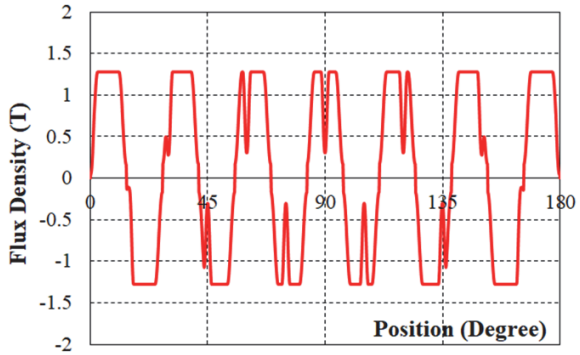

Fig. 21. The air-gap flux density in the 24s/26p M-II MSTPM machine.

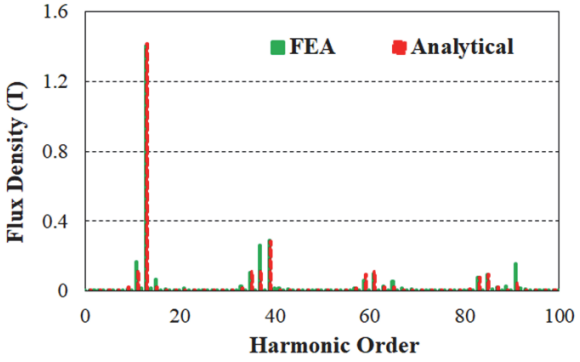

Fig. 22. The air-gap spatial harmonic spectra of the 24s/26p M-II MSTPM machine.

TABLE IV
SPATIAL HARMONICS IN 24S/26P M-II MSTPM MACHINES

Harmonic order	Analytical	2D-FEA
13	1.45 T	1.40 T
37	0.17 T	0.26 T

Furthermore, the 24s/26p M-II MSTPM machine is normalized as the modulation of the PM-MMF, the rotor permeance, and the stator permeance shown in Figs. 18-20, where the amplitude of the PM-MMF is 545.4 A. The analytical air-gap flux density is shown in Fig. 21. The analytical results are compared with the 2D-FEA-predicted results in Fig. 22 and Table IV. According to Table I, the 13-th and 37-th spatial harmonics are the dominant harmonics inducing the fundamental back-EMF in 24s/26p MSTPM machines. It is found that the analytical 13-th harmonic amplitude is close to the 2D-FEA results as well. Also, the difference between analytical and FEA-predicted back-EMF harmonics is acceptable.

C. Phase Back-EMF and Inductance

According to formulae (25) and (26), and Table I, the phase back-EMF can be analytically calculated. In this paper, back-EMF harmonics are ignored in analytical prediction since proposed machines are AC machines, where only fundamental back-EMF can produce electromagnetic torque.

The analytical, FEA-predicted, and tested phase to phase (line) back-EMF waveforms of 48s/52p M-I and 24s/26p M-II MSTPM machines at 480r/min are shown in Fig. 23. The analytical fundamental line back-EMF amplitude of 48s/52p M-I and 24s/26p M-II MSTPM machines are 61 V and 66.5 V,

respectively, and the FEA results considering saturation are 64 V and 65.8 V. When the saturation is ignored, the FEA results of M-I and M-II MSTPM machines are 66 V and 69 V, respectively. The tested fundamental line back-EMF of the two machines are 63.5 V and 65 V. A quite good agreement has been achieved among analytical, FEA, and tested results.

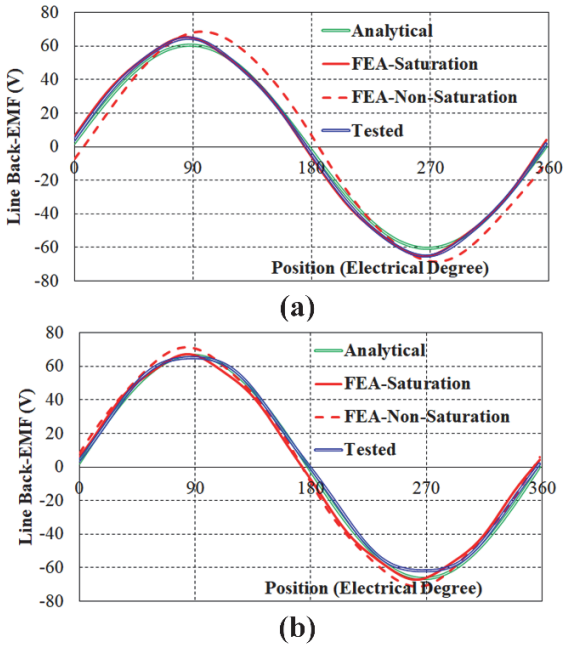

Fig. 23. Line back-EMF waveforms of MSTPM machines at 480r/min. (a) The 48s/52p M-I MSTPM machine. (b) The 24s/26p M-II MSTPM machine.

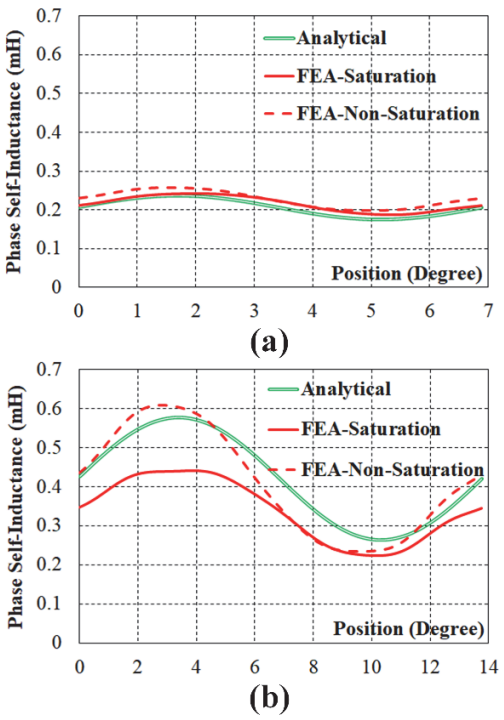

Fig. 24. Phase self-inductance waveforms of MSTPM machines. (a) The 48s/52p M-I MSTPM machine. (b) The 24s/26p M-II MSTPM machine.

The analytical and FEA-predicted phase self-inductance are illustrated in Fig. 24, and the corresponding average inductances are listed in Table V. Besides, the slot leakage component and air-gap component are obtained using analytical model, as shown in Table VI. It is found that the self-inductance of the M-II machine is almost the double of the M-I machine. The slot leakage component is close to the air-gap component in the 48s/52p M-I MSTPM machine, which is 0.106 mH and 0.104 mH, respectively. However, in the 24s/26p M-II MSTPM machine, the air-gap component is quite higher than the slot leakage component, resulting from the large slot width. Besides, the analytical and FEA-calculated mutual-inductance are listed in Table VII. It is found that the 24s/26p M-II MSTPM machine has a more terrible saturation than the 48s/52p M-I MSTPM machine. Overall, a good agreement is achieved.

TABLE V
AVERAGE INDUCTANCE IN MSTPM MACHINES BY DIFFERENT METHODS

Solution	48s/52p M-I	24s/26p M-II
Analytical	0.21 mH	0.42 mH
FEA-Saturation	0.22 mH	0.34 mH
FEA-Non-Saturation	0.23 mH	0.41 mH

TABLE VI
SELF-INDUCTANCE IN MSTPM MACHINES

Components	48s/52p M-I	24s/26p M-II
L_{av}	0.21 mH	0.42 mH
$L_{air\text{-}av}$	0.104 mH	0.37 mH
L_{slot}	0.106 mH	0.05 mH

TABLE VII
MUTUAL-INDUCTANCE IN MSTPM MACHINES

Topologies	Analytical	FEA-Saturation	FEA-Non-Saturation
48s/52p	-0.014 mH	-0.013 mH	-0.013 mH
24s/26p	-0.027 mH	-0.022 mH	-0.027 mH

D. On-load Performance

Based on the back-EMF and inductance, the on-load performance is deduced. In Fig. 25, the analytical, FEA-predicted, and tested torque-current curves of two prototype machines are illustrated and compared. When armature current is less than 30 A, the analytical, FEA, and tested results of the 48s/52p M-I MSTPM machine are very close. When current increases, the error between analytical and FEA & tested results rises since the analytical method ignores the saturation.

As for the 24s/26p M-II MSTPM machine, the analytical, FEA, and tested torque-current curves are very similar throughout the whole current region.

Furthermore, the torque-speed curves of the two MSTPM machines are calculated as shown in Fig. 26. It is found the armature current raises the saturation in the 48s/52p M-I MSTPM machine, resulting in the difference between analytical results and FEA & tested results. Since the analytical model ignores the saturation, the analytical PM flux linkage is higher than the FEA and tested results, the corresponding average torque should be higher when the same current is injected. Further, considering the analytical and FEA inductances are very close, the analytical constant-power region is narrower than the FEA and experimental results. As for the 24s/26p M-II MSTPM machine, the armature current slightly influence the saturation so the analytical, FEA, and tested constant-torque region are similar. However, since the analytical inductance is higher than the FEA-predicted one, the

analytical constant-power region is a bit wider. It is gratifying that the tested results are very close to the FEA-predicted results. Overall, good agreements have been achieved between the analytical, FEA, and tested results.

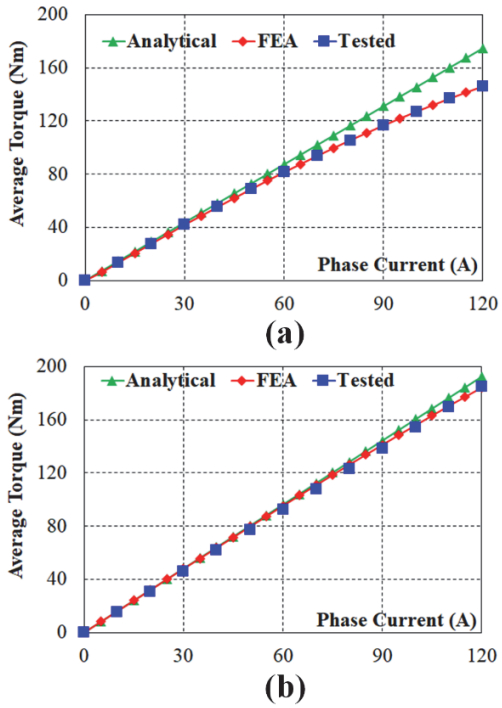

Fig. 25. Torque-current curves of MSTPM machines at 480r/min. (a) The 48s/52p M-I MSTPM machine. (b) The 24s/26p M-II MSTPM machine.

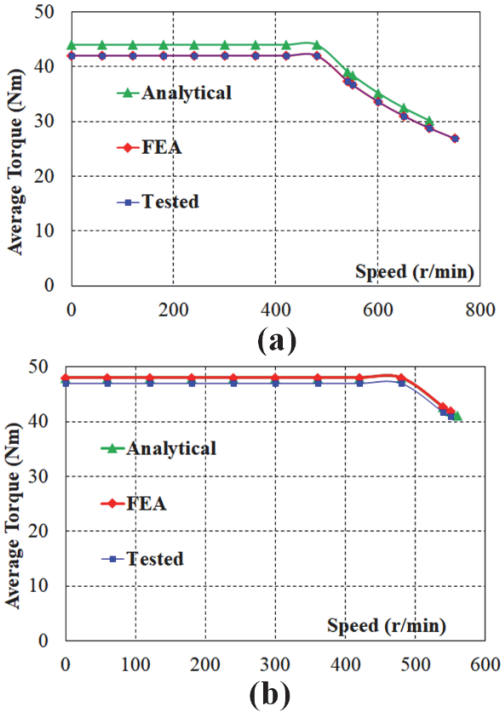

Fig. 26. Torque-speed curves of MSTPM machines at 480r/min. (a) The 48s/52p M-I MSTPM machine. (b) The 24s/26p M-II MSTPM machine.

VI. Conclusion

In this paper, the analytical model of the MSTPM machines is proposed based on the AFM theory. Firstly, the MSTPM machines are divided into three key elements which are the open-circuit PM-MMF, the relative stator permeance, and the relative rotor permeance. The relative stator and rotor permeance are further deduced on the basis of RP model. Then, the general formula is proposed to calculate the back-EMF, as well as discover the relationship between spatial field harmonics and temporal back-EMF harmonics. The winding inductance model of the MSTPM machines for IWT applications are built considering the single-layer and double-layer winding configurations. Finally, the analytical model is verified by FEA-predicted and experimental results of two prototyped machines with different magnetization modes. It is believed that the proposed general model is an effective tool with considerable precision for the design and analysis of the MSTPM machines, especially for in-wheel traction applications.

References

[1] W. Hua, H. Zhang, and et al., "An outer-rotor flux-switching permanent-magnet-machine with wedge-shaped magnets for in-wheel light traction," *IEEE Trans. Ind. Electron.*, vol.64, no.1, pp. 69-80, Jan. 2017.

[2] Y. Yang, M. Rahman, and et al., "Development of an external rotor V-shape permanent magnet machine for E-bike application," *IEEE Trans. Energy Convers.*, vol.33, no.4, pp. 1650-1658, Dec. 2018.

[3] H. Chen, X. Liu, N. Demerdash, et al., "Comparison and design optimization of a five-phase flux-switching PM machine for in-wheel traction applications," *IEEE Trans. Energy Convers.*, vol.34, no.4, pp.1805-1817, Dec. 2019.

[4] X. Xue, K. Cheng, T. Ng, and N. Cheung, "Multi-objective optimization design of in-wheel switched reluctance motors in electric vehicles," *IEEE Trans. Ind. Electron.*, vol.57, no.9, pp. 2980-2987, Sep. 2010.

[5] S. Chung, S. Moon, D. Kim, and J. Kim, "Development of a 20-pole–24-slot SPMSM with consequent pole rotor for in-wheel direct drive," *IEEE Trans. Ind. Electron.*, vol.63, no.1, pp. 302-309, Jan. 2016.

[6] Y. Fan, L. Zhang, J. Huang, and X.D. Han, "Design, analysis, and sensorless control of a self-decelerating permanent-magnet in-wheel motor," *IEEE Trans. Ind. Electron.*, vol.61, no.10, pp. 5788-5797, Oct. 2014.

[7] H. Zhang, W. Hua, and et al., "Modular spoke-type permanent-magnet machine for in-wheel traction applications," *IEEE Trans. Ind. Electron.*, vol.65, no.10, pp.7648-7659, Oct.2018.

[8] H. Zhang, W. Hua, and et al., "Design considerations of novel modular-spoke-type permanent magnet machines," *IEEE Trans. Ind. Appl.*, vol.54, no.5, pp.4236-4245, Sep./Oct. 2018.

[9] H. Zhang, W. Hua, and G. Zhang, "Analysis of back-EMF waveform of a novel outer-rotor-permanent-magnet flux-switching machine," *IEEE Trans. Magn.*, vol.53, no.6, Jun. 2017. Article #:8105004.

[10] H. Zhang, and W. Hua, "The influence of magnetization on modular spoke-type permanent-magnet machine for in-wheel traction applications," *IEEE Trans. Magn.*, vol. 54, no. 11, Nov. 2018. Article #:8105105.

[11] H. Zhang, W. Hua, D. Gerada, et al., "Comparative study on two modular spoke-type PM machines for in-wheel traction applications," *IEEE Trans. Energy Convers.*, vol.34, no.4, pp.2137-2147, Dec. 2019.

[12] M. Cheng, P. Han, and W. Hua, "A general airgap field modulation theory for electrical machines," *IEEE Trans. Ind. Electron.*, vol.64, no.8, pp.6063-6074, Aug. 2017.

[13] H. Wen, and M. Cheng, "Unified analysis of induction machine and synchronous machine based on the general airgap field modulation theory," *IEEE Trans. Ind. Electron.*, vol.66, no.12, pp.9205-9216, May 2019.

[14] Z. Wu, and Z. Zhu, "Analysis of air-gap field modulation and magnetic gearing effects in switched flux permanent magnet machines," *IEEE Trans. Magn.*, vol.51, no.5, May 2015. Article #:8105012.

[15] J. D. McFarland, T. M. Jahns, and A. M. EL-Refaie, "Analysis of the torque production mechanism for flux-switching permanent-magnet

machines," *IEEE Trans. Ind. Appl.*, vol.51, no.4, pp. 3041-3049, Jul. 2015.
[16] M. Cheng, H. Wen, and et al., "Analysis of airgap field modulation principle of simple salient poles," *IEEE Trans. Ind. Electron.*, vol.66, no.4, pp.2628-2638, Apr. 2019.
[17] X. Zhu, W. Hua, and et al., "Analysis of back-EMF in flux-reversal permanent magnet machines by air-gap field modulation theory," *IEEE Trans. Ind. Electron.*, vol.66, no.5, pp.3344-3355, May 2019.
[18] Z. Zhu, and Y. Liu, "Analysis of air-gap field modulation and magnetic gearing effect in fractional-slot concentrated-winding permanent-magnet synchronous machines," *IEEE Trans. Ind. Electron.*, vol.65, no.5, pp.3688-3698, May 2018.
[19] D. Li, T. Zou, and et al., "Analysis of fractional-slot concentrated winding PM vernier machines with regular open-slot stators," *IEEE Trans. Ind. Appl.*, vol.54, no.2, pp. 1320-1330, Mar. 2018.
[20] Z. Wu, and Z. Zhu, "Analysis of magnetic gearing effect in partitioned stator switched flux PM machines," *IEEE Trans. Energy Convers.*, vol.31, no.4, pp. 1239-1249, Dec. 2016.
[21] T. Sheng, S. Niu, and et al., "Topology exploration and torque component analysis of double stator biased flux machines based on magnetic field modulation mechanism," *IEEE Trans. Energy Convers.*, vol.33, no.2, pp. 584-593, Jun. 2018.
[22] Q. Wang, and S. Niu, "A novel hybrid-excited dual-PM machine with bidirectional flux modulation," *IEEE Trans. Energy Convers.*, vol.32, no.2, pp. 424-435, Jun. 2017.
[23] A. Tessarolo, C. Ciriani, and et al., "Investigation into multi-layer fractional-slot concentrated windings with unconventional slot-pole combinations," *IEEE Trans. Energy Convers.*, early access, DOI: 10.1109/TEC.2019.2929950.
[24] A. Tessarolo, "A auadratic-programming approach to the design optimization of fractional-slot concentrated windings for surface permanent-magnet machines," *IEEE Trans. Energy Convers.*, vol.33, no.1, pp. 442-452, Mar. 2018.
[25] H. Zhang, W. Hua, and et al., "The influence of winding location in flux-switching permanent-magnet machines," *IEEE Trans. Magn.*, vol.55, no.7, Jul. 2019. Article #: 8104205.
[26] S. Min, and B. Sarlioglu, "Analysis and comparative study of flux weakening capability in fractional-slot concentrated windings," *IEEE Trans. Energy Convers.*, vol.33, no.3, pp. 1025-1035, Sep. 2018.
[27] B. Gaussens, E. Hoang, and et al., "Analytical Armature Reaction Field Prediction in Field-Excited Flux-Switching Machines Using an Exact Relative Permeance Function," *IEEE Trans. Magn.*, vol. 49, no. 1, pp. 628-641, Jan. 2013.
[28] B. Gaussens, E. Hoang, and et al., "Analytical Approach for Air-Gap Modeling of Field-Excited Flux-Switching Machine: No-Load Operation," *IEEE Trans. Magn.*, vol. 48, no. 9, pp. 2505-2517, Sep. 2012.
[29] A. Hanic, D. Zarko, and Z. Hanic, "A novel method for no-load magnetic field analysis of saturated surface permanent-magnet machines using conformal mapping and magnetic equivalent circuits," *IEEE Trans. Energy Convers.*, vol.31, no.2, pp. 740-749, Jun. 2016.
[30] A. Hanic, D. Zarko, D. Kuhinek, and Z. Hanic, "On-load analysis of saturated surface permanent magnet machines using conformal mapping and magnetic equivalent circuits," *IEEE Trans. Energy Convers.*, vol.33, no.3, pp. 915-924, Sep. 2018.
[31] Q. Lu, B. Wu, and et al., "Analytical model of permanent magnet linear synchronous machines considering end effect and slotting effect," *IEEE Trans. Energy Convers.*, early access, DOI: 10.1109/TEC.2019.2946278.
[32] Z. Zhu, and D. Howe, "Instantaneous magnetic field distribution in brushless permanent magnet dc motors, Part III: effect of stator slotting," *IEEE Trans. Magn.*, vol.29, no.1, pp. 143-151, Jan. 1993.
[33] T.A. Lipo, Introduction to AC Machine Design, Wisconsin Power Electronics Research Center, University of Wisconsin-Madison, 2011.

Hengliang Zhang was born in Anhui, China, in 1992. He received the B.Sc. degree in electrical engineering from Southeast University, Nanjing, China, in 2014. He is currently working toward the Ph.D. degree in electrical engineering with the School of Electrical Engineering, Southeast University, Nanjing, China. From 2018 to 2019, he was with the Power Electronics, Machines and Control Group, The University of Nottingham, Nottingham, U.K., as a Joint-Supervised Ph.D. Student. His research interests include the electromagnetic design, and thermal analysis of permanent magnet machines.

Wei Hua (SM'16) received the B.Sc. and Ph.D. degrees in electrical engineering from Southeast University, Nanjing, China, in 2001 and 2007, respectively. From 2004 to 2005, he was with the Department of Electronics and Electrical Engineering, The University of Sheffield, U.K., as a Joint-Supervised Ph.D. Student. Since 2007, he has been with Southeast University, where he is currently a Chief Professor of Southeast University and a Distinguished Professor of Jiangsu Province. He has co-authored over 150 technical papers. He holds 50 patents in his areas of interest. His teaching and research interests include design, analysis, and control of electrical machines, especially for PM brushless machines and switching reluctance machines, etc.

David Gerada received the Ph.D. degree in high-speed electrical machines from the University of Nottingham, Nottingham, UK in 2012. From 2007-2016 he was with the R&D Department at Cummins, first as an Electromagnetic Design Engineer (2007-2012), and then as a Senior Electromagnetic Design Engineer and Innovation Leader (2012-2016). At Cummins he pioneered the design and development of high-speed electrical machines, transforming a challenging technology into a reliable one suitable for the transportation market, while establishing industry-wide used metrics for such machinery. In 2016 he joined the University of Nottingham as a Senior Fellow in Electrical Machines, responsible for developing state of the art electrical machines for future transportation which push existing technology boundaries, while propelling the new technologies to higher technology readiness levels (TRL). Dr. Gerada is a Chartered Engineer in the U.K. and a member of the Institution of Engineering and Technology.

Zeyuan Xu received the Ph.D. degree in mechanical engineering from the University of Manchester, Manchester, U.K., in 2002. He subsequently worked as a Research Fellow at UMIST, Brunel University, and University of Nottingham. He is currently a Senior Research Fellow in thermo-mechanical design of high-speed electrical machines within the PEMC group at University of Nottingham, Nottingham, U.K. His main research interests include turbulent thermo-fluid flow, heat transfer enhancement, and thermal management of advanced electrical machines and power electronics.

Chris Gerada is an Associate Pro-Vice-Chancellor for Industrial Strategy and Impact and Professor of Electrical Machines. His principal research interest lies in electromagnetic energy conversion in electrical machines and drives, focusing mainly on transport electrification. He has secured over £20M of funding through major industrial, European and UK grants and authored more than 350 referred publications. He received the Ph.D. degree in numerical modelling of electrical machines from The University of Nottingham, Nottingham, U.K., in 2005. He subsequently worked as a Researcher with The University of Nottingham on high-performance electrical drives and on the design and modelling of electromagnetic actuators for aerospace applications. In 2008, he was appointed as a Lecturer in electrical machines; in 2011, as an Associate Professor; and in 2013, as a Professor at The University of Nottingham. He was awarded a Research Chair from the Royal Academy of Engineering in 2013. Prof. Gerada served as an Associate Editor for the IEEE TRANSACTIONS ON INDUSTRY APPLICATIONS and is the past Chair of the IEEE IES Electrical Machines Committee.